

Secondary transfer length and residual prestress of fractured strand in post-tensioned concrete beams

Lizhao DAI^a, Wengang XU^a, Lei WANG^{a*}, Shanchang YI^a, Wen CHEN^b

^a School of Civil Engineering, Changsha University of Science and Technology, Changsha 410114, China

^b Laboratory of Microstructures and Material Mechanics, University of Lorraine, Metz 57045, France

*Corresponding author. E-mail: Leiwang@csust.edu.cn

© Higher Education Press 2022

ABSTRACT An experimental study is performed on five post-tensioned concrete beams to explore the effects of different fracture positions on secondary transfer length and residual prestress of fractured strand. A numerical model is developed and used to predict the secondary transfer length and residual prestress of fractured strand in post-tensioned concrete beams. The model change interaction, which can deactivate and reactivate the elements for simulating the removal and reproduction of parts of the model, is used to reproduce the secondary anchorage of fractured strand. The numerical model is verified by experimental results. Results shows that the fractured strand can be re-anchored in concrete through the secondary anchorage, and the secondary transfer length of fractured strand with the diameter of 15.2 mm is 1133 mm. The residual prestress of fractured strand increases gradually in the secondary transfer length, and tends to be a constant beyond it. When the fractured strand is fully anchored in concrete, a minor prestress loss will appear, and the average prestress loss is 2.28% in the present study.

KEYWORDS post-tensioned concrete beams, strand fracture, secondary transfer length, residual prestress

1 Introduction

Post-tensioned concrete has been widely used in the construction of bridges due to its superior mechanical properties [1,2]. Prestressed strand in concrete is easily affected by stress corrosion during the service period, which may cause the brittle fracture of strand [3–5]. The fractured strand will be re-anchored in concrete along a certain length of the strand, which is termed as the secondary transfer length. Once the prestress is completely transferred, the residual prestress in fractured strand appears [6,7]. The secondary transfer length and residual prestress of fractured strand play an important role in structural safety, which should be investigated further.

The strand after fracture can be re-anchored in grout due to the bond between strand and grout, which was confirmed by Buchner and Lindsell [8]. Zghayar et al. [9] investigated the embedment length of strand that is required to develop the prestressing force. Asp et al. [1]

pointed out that the re-anchoring length of the fractured strand is related to the grout condition. Dai et al. [10] experimentally determined the residual prestressing force of beams based on the cracking load. Unfortunately, no guidance proposed by codes or research is available for evaluation of the secondary transfer length of fractured strand in post-tensioned concrete structures, which requires further study.

The residual prestress of fractured strand plays an important role in the service performance of post-tensioned concrete structures. Rashednia et al. [11] investigated the influence of strand corrosion on the residual prestressing force in prestressed concrete structures. Bagge et al. [12] measured the residual prestressing force in concrete bridges by using *in-situ* methods. However, the existing studies evaluate the residual prestressing force using the indirect methods, such as the cracking moment method, strand-cutting method, which may cause inaccuracy of the results. Additionally, the new anchoring form of fractured strand, i.e., the grout bonded anchoring at one end and anchorage at another end, is complicated. The residual prestress of

fractured strand needs to be studied more deeply.

The purpose of this study is to explore the effects of different fracture positions on the secondary transfer length and residual prestress of fractured strand in post-tensioned concrete beams. This study is arranged as follows. Firstly, an experimental study is performed on five post-tensioned concrete specimens to assess the secondary transfer length and residual prestress of fractured strand. Secondly, a numerical model is developed and used to predict the secondary transfer length and residual prestress of fractured strand. Finally, several conclusions are given.

2 Experimental program

2.1 Details of specimens

Five specimens were designed and manufactured to explore the effects of different strand fracture positions on secondary transfer length and residual prestress of fractured strand in post-tensioned concrete beams. Specimens were divided into two categories: one specimen without the strand fracture (D0) and four specimens with localized fracture of strand (D1, D2, D3, D4). Only one beam was developed for each fracture position of the strand. The effect of variability of materials on experimental results was not considered in the present study. Further studies on the variability of materials are required, but this is outside the scope of the present study. All specimens had a rectangular cross-section of 200 mm × 350 mm, and a length of 4000 mm. A seven-wire strand with a diameter of 15.2 mm was set at the beam bottom. The diameter of metal bellows was 50 mm. Three 10-mm diameter deformed bars were arranged on the beam top as the compressive bar. Three 16-mm diameter deformed bars were arranged at the beam bottom as the tensile bar. The deformed bars with a diameter of 8 mm were used as stirrups. The longitudinal spacing of stirrups was inconsistent, as shown in Fig. 1. The concrete cover of reinforcement bars was 30 mm. Figure 1 shows the details of specimens. The mechanical properties of strand and reinforcement bars are shown in Table 1.

The weight ratios of cement, water, coarse aggregate and fine aggregate were 1:0.45:2.89:2.06 in the concrete mixture, conforming to the Chinese Technical Specification JGJ 55-2011 [13]. All specimens were cast in one batch. Three cubic samples with the dimension of 150 mm × 150 mm × 150 mm were cast. A uniaxial compressive test was performed to obtain the compressive strength of concrete. The average 28-d compressive strength of concrete was 46.6 MPa. To avoid the elastic shortening of grout, high-strength non-shrink grout was adopted. The weight ratios of grouting material and water were 1:0.33 in grout mixture. Three cubic samples with the dimension of 70 mm × 70 mm × 70 mm were cast to obtain the compressive strength of the grout according to Chinese code GB/T 25181-2019 [14]. The average 28-d compressive strength of the grout was 40.3 MPa.

2.2 Strand fracture test

Stress corrosion can induce the brittle fracture of strand in corroded post-tensioned concrete structures during the service period. To simulate the brittle fracture of strand, the strand in concrete was sawn in this study. A cavity with the size of 30 mm × 125 mm × 70 mm was reserved in specimens before casting, as shown in Fig. 1. The strand in cavity was sawn after the curing of concrete and grout. Four different fracture positions of strands were selected. The strand of D1 was sawn in anchorage region. The strand of D2 was sawn in $L/4$ region (where L was the length of specimen). The strand of D3 was sawn in $3L/8$ region. The strand of D4 was sawn in mid-span region. The strand fracture position in each specimen is shown in Fig. 2.

2.3 Measurement of residual prestress and transfer length

In this study, the residual prestress of fractured strand in specimens was obtained using the anchor load cell at the end of specimens, as shown in Fig. 2. Some previous experimental studies used the strain of strand in longitudinal direction to assess the transfer length [9, 15–17]. Therefore, in this work, the secondary transfer length after strand fracture was evaluated by the change of strand strain as well. Coronelli et al. [18] found that

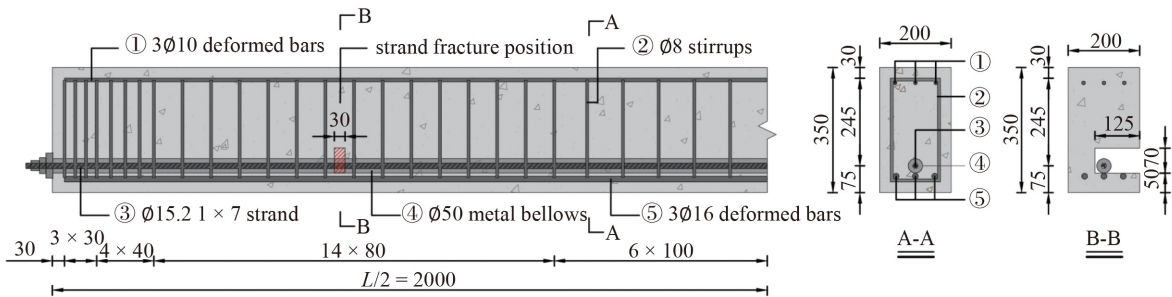


Fig. 1 Details of specimens (unit: mm).

strain gauges were easily broken near the fracture position after the strand fracture. The strain gauges were stuck on the surface of the metal bellows to obtain the strain data of strand indirectly and so to avoid the failure of strain gauges [9]. According to ACI 318-14 [19] and JTG 3362-2018 [20], the transfer lengths of seven-wire strand with the diameter of 15.2 mm were 1024 and 972 mm, respectively. Therefore, the strain gauges were densely arranged in the region between 900 and 1300 mm and sparsely arranged in other regions, as shown in Fig. 2.

2.4 Static loading test

A static loading test was performed to investigate the cracking and the ultimate loads of specimens with different strand fracture positions. The four-point flexural test was conducted on all specimens. The pure-flexural span and the shear-flexural span of specimens were 1000 and 1300 mm, respectively. The load was applied monotonically on the specimens, which was measured by the load cell. Five dial gauges were used to measure the vertical displacement at loading points, supports and mid-span section. The distribution of cracks was described

using $50 \text{ mm} \times 50 \text{ mm}$ grids marked on each side of specimens. Figure 3 shows the diagram of load device.

3 Experimental results and discussion

3.1 Secondary transfer length after strand fracture

The fractured strand retracts along the longitudinal direction of beams. At first, the retraction force is transferred to the grout under the action of the interfacial forces at the strand-grout interface. After that, the retraction force is transferred to the metal bellows under the action of the interfacial forces at the interface of grout-metal bellows. Finally, the retraction force is transferred to concrete under the action of the interfacial forces at metal bellows-concrete interface. The fractured strand is re-anchored in concrete under the above action. The prestress in fractured strand is transferred to concrete along a certain length of the strand, which is termed as the secondary transfer length. The definition of “secondary transfer length” used is specific to prestress transfer in post-tensioned concrete beams after strand fracture in the present study. The secondary transfer length is similar to the transfer length in pretensioned concrete beams, but not the transfer length.

The secondary transfer length of each fractured strand is determined by the metal bellow strain profiles along with the 95% Average Maximum Strain method, as shown in Fig. 4. The detail of the 95% Average Maximum Strain method can be found in Russell and

Table 1 Mechanical properties of reinforcement bars and strand

type	diameter (mm)	yield strength (MPa)	ultimate strength (MPa)	elastic modulus (GPa)
tensile bar	16	400	540	200
compressive bar	10	400	540	200
stirrup	8	300	420	210
strand	15.2	1860	1910	195

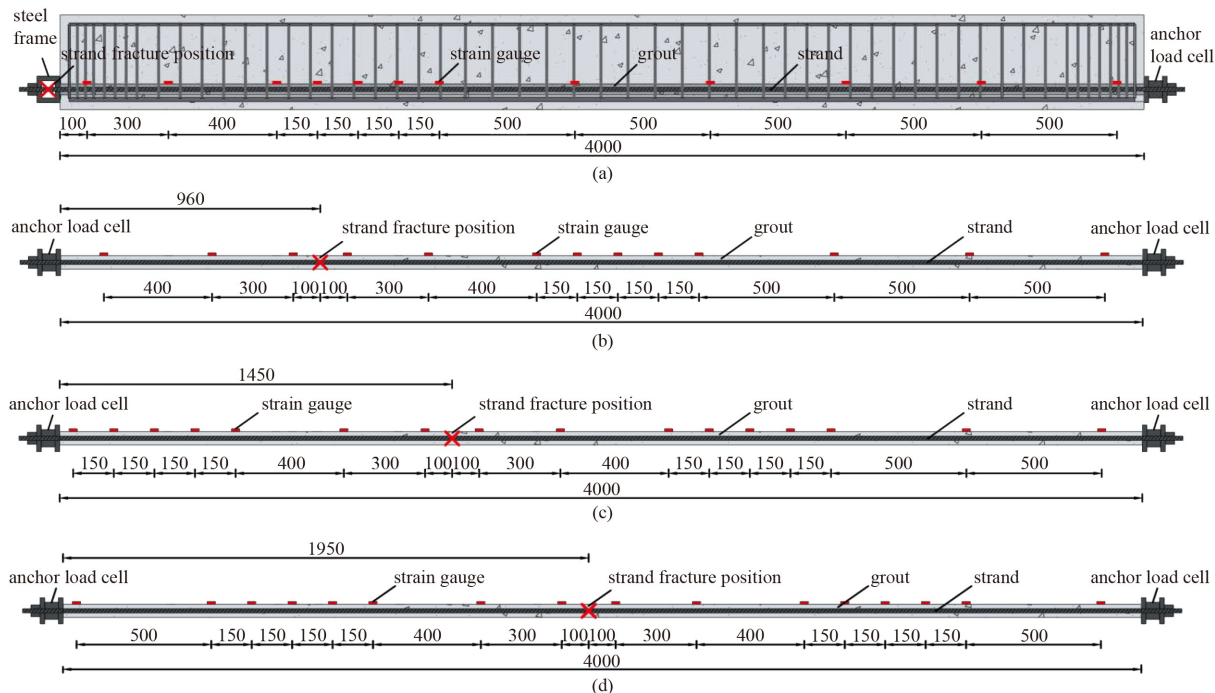


Fig. 2 Positions of strand fracture and strain gauges (unit: mm): (a) D1; (b) D2; (c) D3; (d) D4.

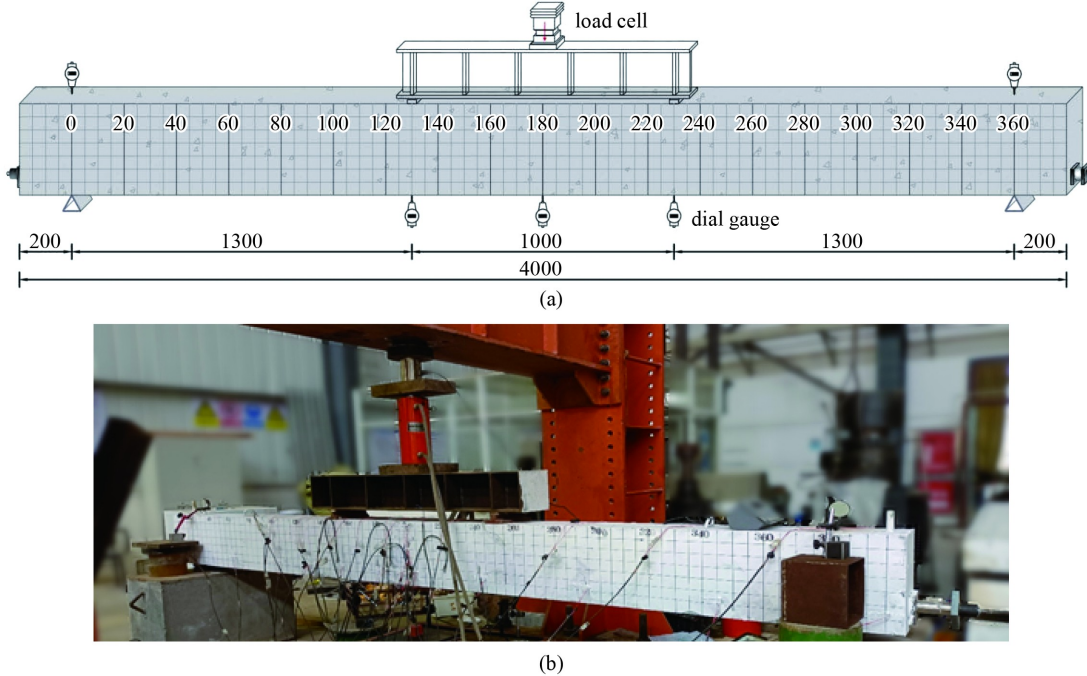


Fig. 3 Diagram of load device (unit: mm): (a) schematic diagram; (b) photo.

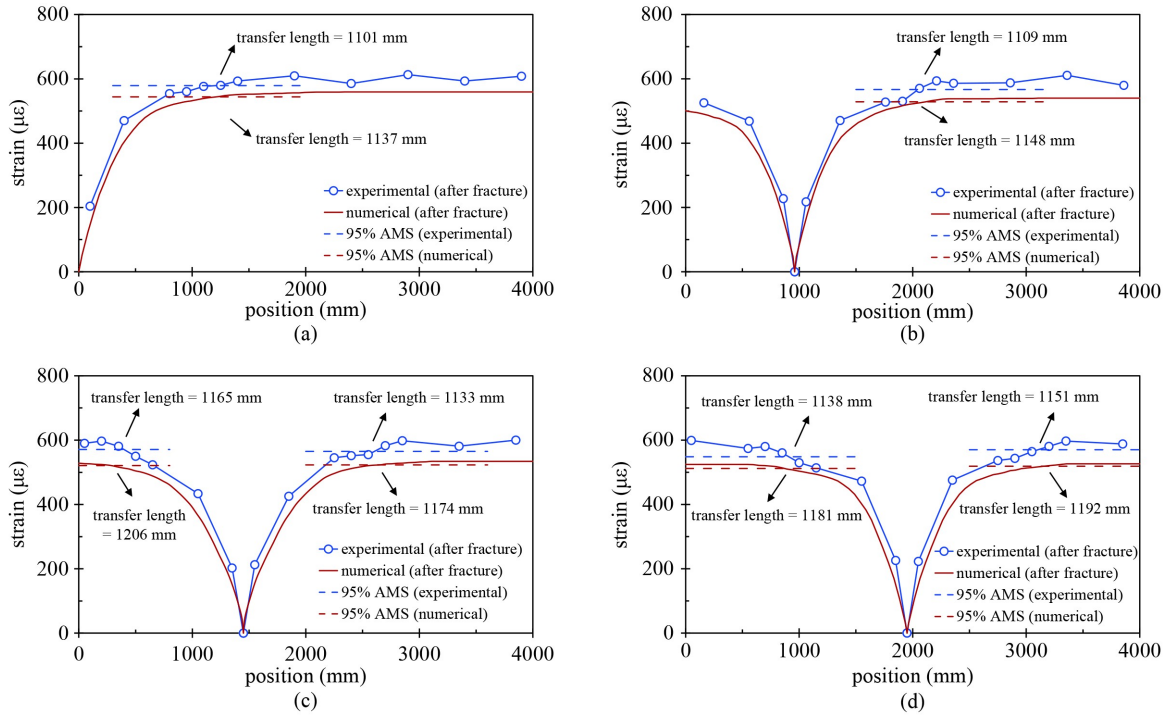


Fig. 4 Experimental and numerical strains: (a) D1; (b) D2; (c) D3; (d) D4.

Burns [21]. This method is widely employed by many scholars for evaluating the transfer length [16,22,23]. As Fig. 4 shows, the secondary transfer length of fractured strand ranges from 1101 to 1165 mm. The average value of 1133 mm is used to reflect the secondary transfer length in this study.

Figure 4 shows that the different transfer mechanism is determined by the different strand fracture positions.

Only one transfer zone in the secondary anchorage is formed as the strand fractures in the anchorage region (D1). Two transfer zones in the secondary anchorage are formed once the strand fractures in other positions (D2, D3, D4). The strain at the fractured position decreases to zero, which means that the prestress at strand fracture position is entirely lost. The strain of the fractured strand to the left of D2 increases steadily, which is different

from the cases of D3 and D4. This indicates that when the beam length in one side after strand fracture is smaller than the secondary transfer length then the stabilization stage of strand strain will not appear.

3.2 Residual prestress of fractured strand

The fractured strand will rebuild the new prestress through the secondary anchorage. Table 2 shows the change of effective prestress in strand at different stages. The effective prestress before strand fracture decreases by a certain degree as compared to the initial prestress, and the average prestress loss ρ_1 is 1.04%. The prestress loss at this stage may be attributed to the elastic shortening of the grout, anchorage loss, frictional loss and time-dependent loss. After strand fracture, the residual prestress will be rebuilt through the secondary anchorage. As shown in Table 2, the residual prestress after strand fracture decreases by a certain degree as compared to the effective prestress before strand fracture. The prestress loss ρ_2 in the secondary anchorage is determined by the strand fracture position. When the fractured strand can be fully anchored in the beam, the average prestress loss ρ_2 of fractured strand is 2.28%. It should be noted that the prestress loss ρ_2 of D2 (left) is 6.55%, which is nearly three times that of the other fractured strands. This is due to the fact that the length of fractured strand is only 945 mm, such that the fractured strand cannot be fully anchored in the beam. The average value of 1049 MPa is

used to reflect the residual prestress of fractured strand in the present study.

3.3 Cracking and ultimate loads after strand fracture

The redistribution of prestress in fractured strand can influence the cracking and the ultimate loads of beams. The cracking and the ultimate loads of beams at different strand fracture positions are investigated by a static loading test. The mid-span displacement is adopted to represent the deflection of specimens in the following analysis. Figure 5(a) illustrates the load–deflection curves of specimens.

As shown in Fig. 5(a), the load–deflection curves of specimens are divided into three stages according to the cracking and yield loads. The load–deflection curves have the similar deformation behavior in the first stage before the cracking load. This indicates that the effect of strand fracture on stiffness can be ignored in this region. The flexural stiffness of un-cracked specimens is determined by the moment of inertia of the cross-section of concrete. The curve slopes of beams with strand fracture are less than that of D0 after the cracking load. This indicates that the strand fracture causes the stiffness degradation of specimens after concrete cracking. When the strand fracture position moves towards the mid-span region, the degree of stiffness degradation increases. The deflection of specimens increases rapidly under a small increase of applied load after the yield load in the third

Table 2 Change of effective prestress in strand at different stages

type	D0	D1	D2 (left)	D2 (right)	D3 (left)	D3 (right)	D4 (left)	D4 (right)
initial prestress (MPa)	1124	1119	1090	1090	1084	1084	1089	1089
effective prestress before strand fracture (MPa)	1115	1109	1079	1079	1069	1069	1077	1077
prestress loss ρ_1 (%)	0.80	0.96	0.98	0.98	1.32	1.32	1.12	1.12
residual prestress after strand fracture (MPa)	–	1087	1009	1039	1046	1049	1061	1051
prestress loss ρ_2 (%)	–	1.94	6.55	3.77	2.17	1.87	1.53	2.39

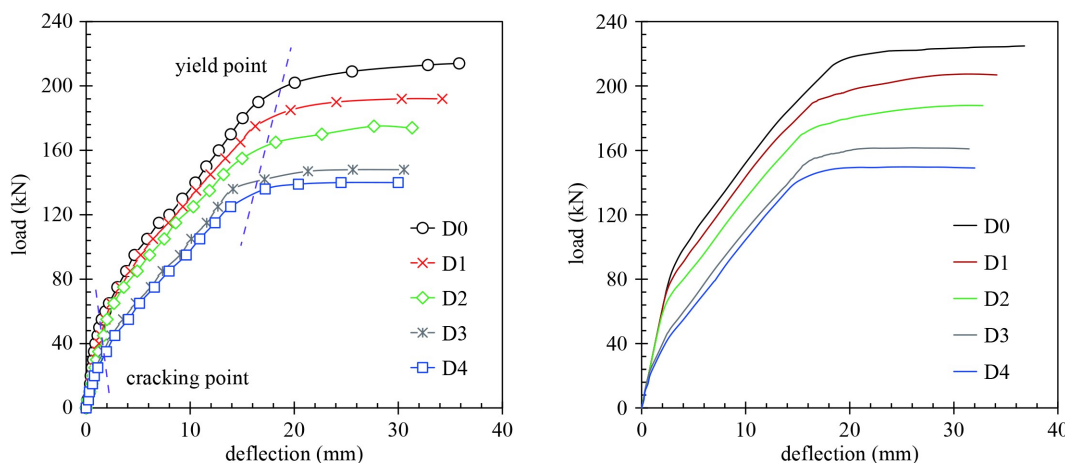


Fig. 5 Load–deflection curves of specimens: (a) experimental results; (b) numerical results.

region. Finally, the specimen fails once the main crack exceeds the critical width or the concrete crushing in the compression zone.

The cracking and ultimate loads of specimens are given in [Table 3](#). The cracking loads of D1, D2, D3, and D4 decrease by 8.20%, 32.79%, 50.82%, and 59.02% as compared to D0, respectively. As the strand fracture position moves towards the mid-span region, the cracking load decreases gradually. For D1, the tensile stress generated by the applied load in the anchorage region can be negligible. Therefore, the strand fracture in the anchorage region has little effect on the concrete cracking of specimens. The cracking load of D1 is similar with that of D0. For the other specimens, the prestress of fractured strand at fracture position is null and the tensile stress generated by applied load increases. The crack will occur earlier near the strand fracture region than in the mid-span region, which leads to the decrease of cracking load. As the strand fracture position moves towards the mid-span region, a greater decrease of cracking load will occur.

The ultimate load of specimen is represented by the maximum applied load in this study. As illustrated in [Table 3](#), the ultimate loads of D1, D2, D3, and D4 decrease by 10.28%, 18.22%, 30.84%, and 34.58% as compared to D0, respectively. As the strand fracture position moves towards the mid-span region, the ultimate load of the specimen decreases progressively. The difference in the ultimate load for different specimens is connected to the change of the damage control section. For D0 and D1, the tensile stress is generated due to the occurrence of the fastest increase of the applied load in the mid-span section. The damage control section appears in the mid-span region. The failure mode is concrete crushing failure. For the other specimens, the tensile stress at the strand fracture position increases rapidly under the applied load. Meanwhile, the capacity of concrete for resisting the tensile stress at the fracture position decreases. This causes the failure of specimens to occur at the strand fracture region earlier than in the mid-span region. The damage control section changes from the mid-span region to the strand fracture region, and the failure mode changes to the main crack failure. A

further degradation of ultimate load will appear as the strand fracture position approaches the mid-span region.

4 Numerical simulations of secondary anchorage after strand fracture

4.1 Numerical model generation

A numerical model is developed and used to predict the secondary transfer length and the residual prestress of fractured strand, as shown in [Fig. 6\(a\)](#). The following assumptions are made to simplify the numerical model: 1) the ideal elastoplastic models are adopted for the constitutive model of strand and reinforcement bars; 2) the helical-shaped of strand is simplified to a circle according the principle of equal cross-sectional area; 3) the reinforcement bars are perfectly bonded to the concrete; 4) there is no relative slip between the concrete and the grout.

Concrete, reinforcement bar, prestressed strand and grout are simulated using different element types. The rectangular metal gaskets are set at the support to avoid the distortion of elements, and then each part is assembled. Concrete and grout are modelled with eight-node hexahedral elements, and reinforcement bar and strand are modelled with the two-node linear three-dimensional truss elements.

The concrete damage plasticity (CDP) model proposed by Lubliner et al. [24] is adopted for modelling the constitutive model of components (including concrete and grout) ([Fig. 6\(b\)](#)). The failure of concrete can be simulated with the constitutive model of concrete containing plastic strain, which is controlled by the equivalent tensile plastic strain $\bar{\varepsilon}_c^{pl}$ and the equivalent compressive plastic strain $\bar{\varepsilon}_c^{pl}$ [25]. Dai et al. [25] and Xiong et al. [26] have also used the CDP model to simulate the constitutive model of concrete. The plastic strain of the concrete is considered in the constitutive model. Therefore, the present study uses the same CDP model, which contains the plastic strain, to simulate the constitutive model of concrete. The yield surface function proposed by Lubliner et al. [24] is adopted in the CDP model. The invariant stress ratio K_c and biaxial/uniaxial compression plastic strain ratio f_{b0}/f_{c0} are 0.667 and 1.16, respectively. The damage to the concrete is investigated by introducing the damage variable d_t and d_c into the CDP model. d_t and d_c are the damage variables in tension and compression, which may range from 0 to 1.0, where 0 represents no damage and 1.0 represents complete damage. Viscosity parameter μ is adopted for the viscoplastic regularization of the concrete constitutive equation. μ is taken as zero for concrete [27]. More details of the parameters can be found in Xiong et al. [26]. The stress-strain relationship ($\sigma - \varepsilon$) of components under

Table 3 Cracking and ultimate loads of specimens

type	cracking load (kN)	position of the first crack	ultimate load (kN)	failure mode
D0	61	mid-span region	214	concrete crushing failure
D1	56	mid-span region	192	concrete crushing failure
D2	41	strand fracture position	175	main crack failure
D3	30	strand fracture position	148	main crack failure
D4	25	strand fracture position	140	main crack failure

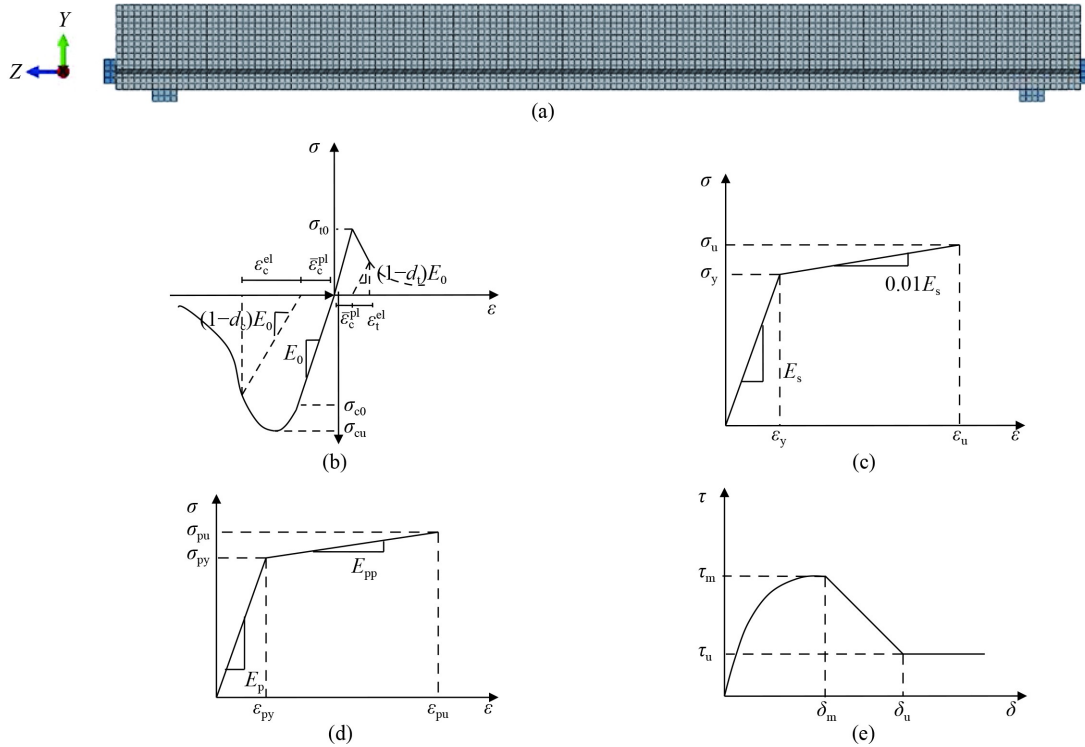


Fig. 6 Numerical simulation: (a) model; (b) uniaxial stress–strain curves of components in CDP model; (c) stress–strain of reinforcement bars; (d) stress–strain of strand and (e) bond stress–slip.

compression and tension is given in Eqs. (1) and (2).

$$\sigma_c = (1 - d_c)E_0(\varepsilon_c - \bar{\varepsilon}_c^{pl}), \quad (1)$$

$$\sigma_t = (1 - d_t)E_0(\varepsilon_t - \bar{\varepsilon}_t^{ck}), \quad (2)$$

where σ_c and σ_t are stresses of components in compression and tension; ε_c and ε_t are the strains of components in compression and tension; $\bar{\varepsilon}_c^{pl}$ is the equivalent plastic strain of components in compression; $\bar{\varepsilon}_t^{ck}$ is the cracking strain of components; E_0 is the elastic modulus of components.

Several numerical methods have previously been proposed for modelling the fracture of reinforced concrete, such as the cracking-particle method [28,29], the adaptive meshfree method [30], the three-dimensional cohesive crack method [31], the dual-horizon peridynamics method [32], the nonlocal operator method [33–35], and the explicit phase field method [36,37]. It is most realistic to consider the fracture simulation of reinforced concrete in the numerical model. However, the present study focuses on the secondary transfer length and residual prestress of fractured strand. The damage to concrete is reflected by introducing the damage variables into the CDP model. Further studies on the fracture simulation of reinforced concrete are needed.

The bilinear constitutive model proposed by Li et al. [38] is adopted for the stress-strain relationship of reinforcement bars (Fig. 6(c)), which can be expressed as

$$\sigma = \begin{cases} E_s \varepsilon, & \varepsilon < \varepsilon_y, \\ \sigma_y + 0.01E_s(\varepsilon - \varepsilon_y), & \varepsilon \geq \varepsilon_y, \end{cases} \quad (3)$$

where σ_y and ε_y are the yield strength and the yield strain of reinforcement bars; E_s is the elastic modulus of reinforcement bars.

The bilinear constitutive model proposed by Wang et al. [39] is adopted for the stress-strain relationship of prestressed strand (Fig. 6(d)), which can be expressed as

$$\sigma = \begin{cases} E_p \varepsilon, & \varepsilon < \varepsilon_{py}, \\ \sigma_{py} + 0.01E_{pp}(\varepsilon - \varepsilon_{py}), & \varepsilon \geq \varepsilon_{py}, \end{cases} \quad (4)$$

where σ_{py} and ε_{py} are the yield strength and the yield strain of strand, respectively; E_p and E_{pp} are the elastic modulus and the hardening modulus of strand, respectively.

To determine the appropriate mesh size, a mesh sensitivity analysis is conducted in the present study. The uniform mesh is used for the meshing of the numerical model. Taking the D0 and D4 as examples, the numerical model is meshed with three sizes (20, 25, and 30 mm). The load–deflections of D0 and D4 are shown in Fig. 7. The results of the model with the meshing of 20 and 25 mm are almost identical, while the results of the model with the meshing of 30 mm have a small deviation. To reduce the computational cost, the numerical model is established with the meshing of 25 mm. The number of elements of concrete, grout, strand and reinforcement bars is 17280, 636, 159, and 2904, respectively.

Numerous studies have found that it would be more reasonable to consider the critical energy release rate in the numerical model, which can ensure mesh independence [23,40]. However, the present study focuses on the simulation of the strand fracture using the model change interaction. The critical energy release rate is not considered in the present study, which will be studied further. The material parameters of the numerical model are given in Table 4.

4.2 Simulation of interfacial bond slip

The two-node nonlinear spring element is a special function element of ABAQUS, which can simulate the relative slip of two nodes. Therefore, the interfacial elements between strand and grout are modelled using the two-node nonlinear springs for simulating the interfacial bond slip, as shown in Fig. 8. The nonlinear spring has two nodes, which are connected to the grout and the strand. Nonlinear springs are established in x -axis, y -axis, and z -axis directions, and the nonlinear spring stiffness in x -axis and y -axis directions are set to infinite. This means that only relative displacement between the two nodes of the nonlinear spring in the z -direction is allowed, i.e., the

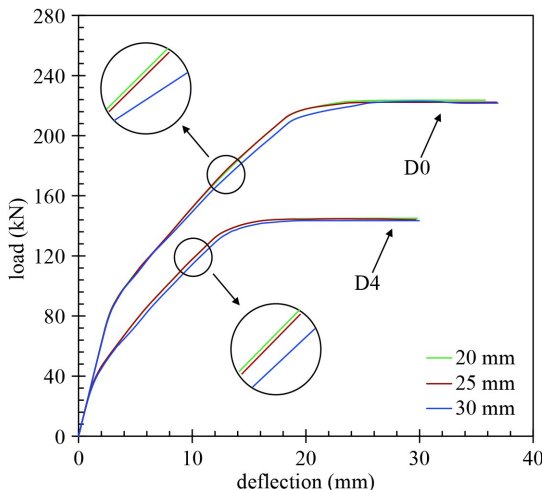


Fig. 7 Load-deflection curves of D0 and D4 (numerical results).

Table 4 Material parameters of the numerical model

type	concrete	grout	strand	tensile bar	compressive bar	stirrup
Young's modulus E (GPa)	33.5	32.4	195	200	200	210
Poisson ratio ν	0.2	0.2	0.3	0.3	0.3	0.3
tensile strength f_t (MPa)	2.51	2.38	—	—	—	—
compressive strength f_c (MPa)	46.6	40.3	—	—	—	—
dilation angle ψ	30	30	—	—	—	—
eccentricity η	0.1	0.1	—	—	—	—

slip between grout and strand will only occur along the longitudinal direction of the strand. The interfacial bond slip only occurs between strand and grout, the reinforcement bars are embedded in the concrete.

The bond stress-slip model of strand proposed by Wang et al. [41] is adopted in this numerical model (Fig. 6(e)). The model can be divided into three different stages: 1) nonlinear increase stage; 2) linear decrease stage; 3) constant residual strength stage, which can be expressed as:

$$\tau = \begin{cases} \tau_m \left(\frac{\delta}{\delta_m} \right)^a, & 0 \leq \delta \leq \delta_m, \\ \tau_m - (\tau_m - \tau_u) \left(\frac{\delta - \delta_m}{\delta_u - \delta_m} \right), & \delta_m < \delta \leq \delta_u, \\ \tau_u, & \delta_u < \delta, \end{cases}, \quad (5)$$

where the maximum bond stress τ_m is taken as $1.25 \sqrt{f_{ck}}$; the residual bond stress τ_u is taken as $0.4\tau_m$; f_{ck} is the characteristic compression stress of the concrete; the slip corresponding to the maximum bond stress δ_m and the slip corresponding to the residual bond stress are taken as 3 and 12 mm, respectively; the constant parameter is taken as 0.4.

The bond stress-slip curve is divided into microsegments. Assuming that each micro-segment is small enough, the bond stress within each microsegment remains the same, i.e., the spring stiffness in each microsegment is the same. In accordance with the consistency of spring force and interfacial force in each microsegment, the spring stiffness $K(\delta_i)$ corresponding to the slip of δ_i can be expressed as

$$K(\delta_i) = \frac{\tau(\delta_i)C_p l_p}{d\delta_i}, \quad (6)$$

where $\tau(\delta_i)$ is the bond strength of strand with the slip of δ_i ; C_p is the perimeter of the strand; l_p is the length of strand contained in each spring.

4.3 Simulation of strand fracture

Prestressed strand under the high stress state is easily affected by stress corrosion. Stress corrosion may cause the brittle fracture of a strand, which changes the anchoring form of fractured strand. The new anchoring form of fractured strand, i.e., the grout bonded anchoring at one end and the anchorage anchoring at another end, is different from that of post-tensioned concrete beams. A model change interaction in ABAQUS makes it possible to deactivate and reactivate elements for simulating removal and reproduction of part of the model, either temporarily or for the remainder of the analysis. Therefore, the fracture of the strand is simulated by model change interaction. To avoid the slip of strand caused by prestressing before strand fracture, the grout element is deactivated before the simulation of

prestressing. The prestress of strand is simulated by the cooling method. The reduced temperature (ΔT) can be expressed as

$$\Delta T = \frac{N_p}{\alpha E_p A_p}, \quad (7)$$

where N_p is the initial prestressing force of strand; α is the thermal coefficient of expansion, which is taken as $1.2 \times 10^{-5} \text{ }^{\circ}\text{C}^{-1}$; E_p is the elastic modulus values of strand; A_p is the cross-sectional area of strand.

The fractured strand will retract towards the end of the test beam, which causes the slip between grout and fractured strand. The interfacial bond slip between grout and fractured strand is simulated in the model, based on the bond stress-slip model of strand and the nonlinear springs. The numerical model established by the above

methods can simulate the whole process of the secondary anchorage after strand fracture. The simulation steps for the whole process of strand fracture are shown in Fig. 9.

4.4 Model validation

The experimental results are employed to validate the proposed numerical model. The strand is only subjected to interfacial force and prestress in the longitudinal direction due to the strand adopts the two-node linear three-dimensional truss element. This causes the strand to generate strain only longitudinally. The secondary transfer length of fractured strand can be obtained indirectly by the change of strain in the longitudinal direction of the grout in the model. Figure 4 shows the experimental and numerical strain curves after strand fracture.

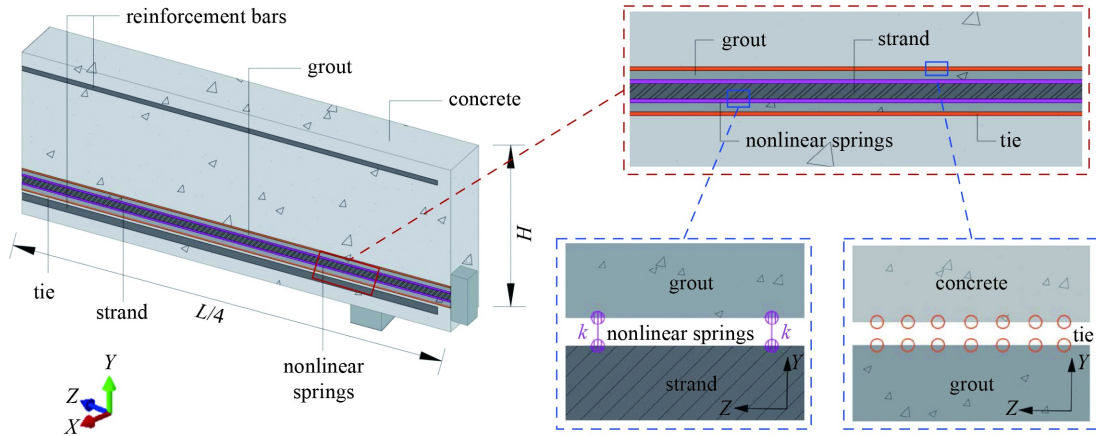


Fig. 8 Interactions of concrete-grout interface and grout-strand interface.

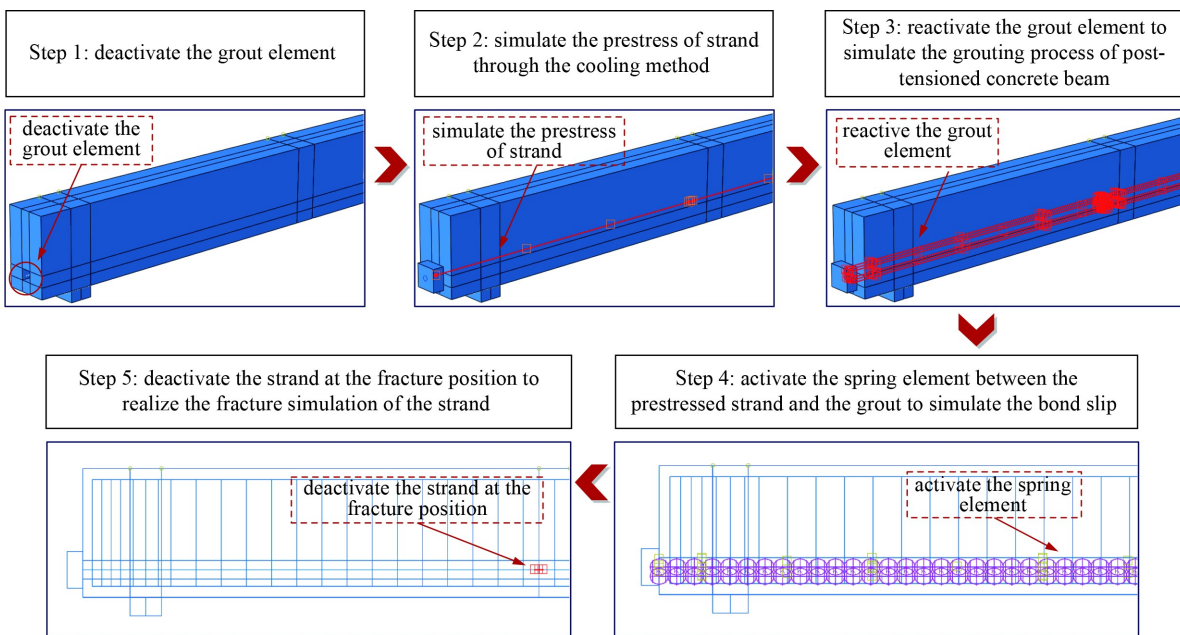


Fig. 9 Simulation steps of strand fracture.

As shown in Fig. 4, after the strand fracture, the strain of the other fractured strands tends to stabilize after a certain distance, except for the fractured strand on the left side of D2. This indicates that the fractured strand will be re-anchored in the beam through the secondary anchorage. The experimental and numerical secondary transfer lengths are compared in Table 5. The average relative error between the experimental and the numerical results is 3.5%, which indicates that the numerical secondary transfer lengths show a good agreement with the experimental secondary transfer lengths.

The change of stress along the strand direction is shown in Fig. 10. The longitudinal stress of fractured strand increases gradually from the fractured region, and finally becomes constant beyond the transfer length. The constant stress beyond the transfer length can be considered to be the residual prestress of fractured strand. Figure 10 shows the experimental and numerical residual prestress in fractured strand. The numerical results approximate adequately to the experimental results. The average error is 2.5%. The relative errors can be accepted as being within the range that may be caused by the variability of materials. The numerical model proposed in this study

can accurately predict the residual prestress in fractured strand.

Figure 5(b) shows the numerical results of the load–deflection curves of specimens. As shown in Fig. 5(b), the numerical simulation can reproduce the experimental results very well. It is thought that some difference between the numerical and experimental results is due to the variability of materials. The concrete damage contours for tensile stress of D4 with different mesh sizes are shown in Fig. 11, which is corresponding to the damage exceeding the crack strain. The simulated tensile deformations of D4 with different mesh sizes are the same. This indicates that the different mesh sizes have little influence on the damage to the beam.

Taking the fractured strand on the left of the fracture position as an example, the effects of different fracture positions on secondary transfer length and residual prestress of fractured strand are investigated (Fig. 12). The length of secondary transfer zone becomes a constant as the length of fractured strand exceeds the critical value, which is called the secondary transfer length. The residual prestress of fractured strand depends on the strand fracture position. When the length of fractured

Table 5 Experimental and numerical secondary transfer lengths of fractured strand

type	D1	D2 (left)	D2 (right)	D3 (left)	D3 (right)	D4 (left)	D4 (right)
experimental results (mm)	1101	960	1109	1165	1133	1138	1151
numerical results (mm)	1137	960	1148	1206	1174	1181	1192
relative error (%)	3.3	–	3.5	3.5	3.6	3.8	3.6

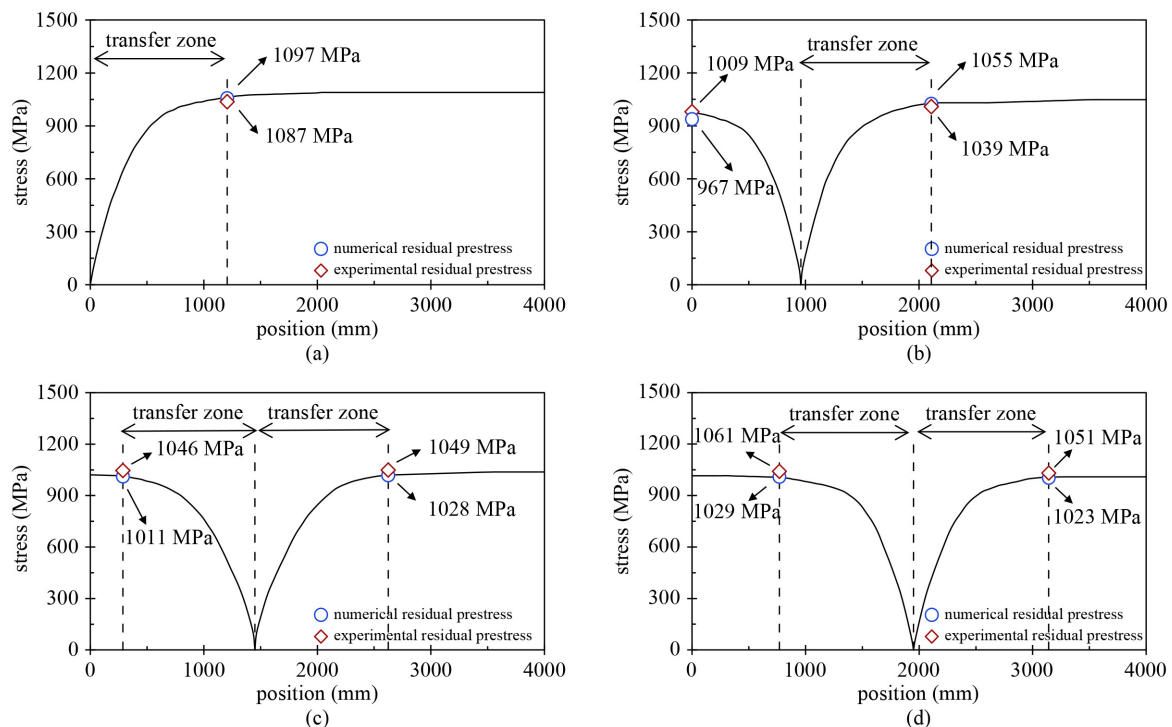


Fig. 10 Longitudinal stress distribution of fractured strand in numerical model: (a) D1; (b) D2; (c) D3; (d) D4.

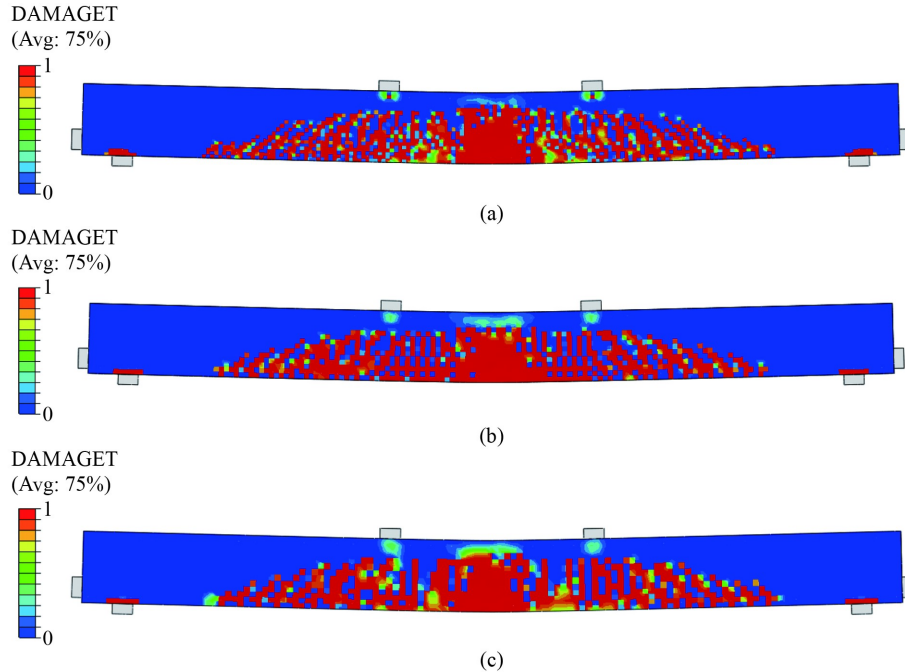


Fig. 11 The damage of D4 with different mesh sizes: (a) 20 mm; (b) 25 mm; (c) 30 mm.

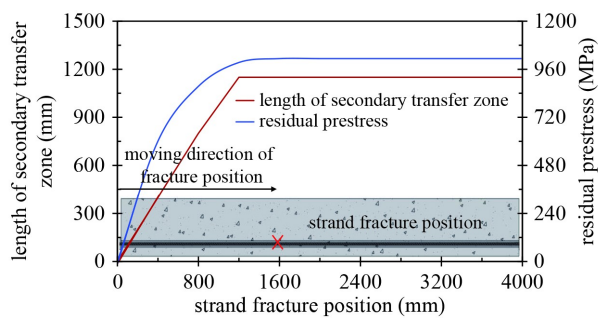


Fig. 12 Length of secondary transfer zone and residual prestress of fractured strand.

strand is less than the secondary transfer length, the fractured strand cannot be fully anchored in grout due to insufficient bond capacity. This causes the residual prestress in fractured strand to be much lower than initial effective prestress. Once the length of fractured strand exceeds the secondary transfer length, the fractured strand can be fully anchored in concrete, and a minor prestress loss of fractured strand will appear.

5 Conclusions

An experimental study is performed on five post-tensioned concrete specimens to explore the secondary transfer length and residual prestress of fractured strand. A numerical model using the model change interaction, which can deactivate and reactivate the elements for simulating the removal and reproduction of parts of the model, is established to reproduce the secondary

anchorage of fractured strand. The following conclusions are drawn.

1) A fractured strand can be re-anchored in concrete under the action of the secondary anchorage. The secondary transfer length of fractured strand with the diameter of 15.2 mm is 1133 mm.

2) The residual prestress distribution of fractured strand depends on the strand fracture positions. The residual prestress of fractured strand increases gradually in the secondary transfer length, and tends to be a constant beyond it. When the fractured strand is fully anchored in concrete, a minor prestress loss will appear, and the average prestress loss is 2.28% in this study.

3) The cracking and ultimate loads of beams degrade gradually as the strand fracture position moves from the anchorage region to the mid-span region. The cracking and ultimate loads decrease by 59.02% and 34.58%, respectively, as the strand fractures at the mid-span region.

4) The innovation of the proposed numerical model is that it uses the model change interaction to simulate the secondary anchorage of fractured strand. Results show that the proposed model can predict, with reliability, the secondary transfer length and residual prestress of fractured strand.

It should be indicated that the strand in concrete is sawn in this study to simulate the brittle fracture of prestressed strand, which may not be consistent with fracture due to natural corrosion. Additionally, the proposed model ignores the interfacial bond slip between reinforcement bars and concrete. The above factors should be investigated further.

Acknowledgements This work was supported by the National Natural Science Foundation of China (Grant No. 52008035), the Science Fund for Creative Research Groups of Hunan Province (No. 2020JJ1006), the Science and Technology Innovation Program of Hunan Province (No. 2020RC4024), the Special Funds for the Construction of Innovative Provinces in Hunan Province (No. 2019SK2171), the Natural Science Foundation of Hunan Province (No. 2021JJ40574), and National-Local Joint Laboratory of Engineering Technology for Long-term Performance enhancement of Bridges in Southern District (Changsha University of Science & Technology) (No. 19KB03). Their supports are gratefully acknowledged.

References

- Asp O, Tulonen J, Kuusisto L, Laaksonen A. Bond and re-anchoring tests of post-tensioned steel tendon in case of strand failure inside cement grouting with voids. *Structural Concrete*, 2021, 22(4): 2373–2390
- Gkantou M, Theofanous M, Baniotopoulos C. A numerical study of prestressed high strength steel tubular members. *Frontiers of Structural and Civil Engineering*, 2020, 14(1): 10–22
- Li D S, Tan M L, Zhang S F, Ou J P. Stress corrosion damage evolution analysis and mechanism identification for prestressed steel strands using acoustic emission technique. *Structural Control and Health Monitoring*, 2018, 25(8): e2189
- Nürnberg U. Corrosion induced failure mechanisms of prestressing steel. *Materials and Corrosion*, 2002, 53(8): 591–601
- Zhang W P, Liu X G, Gu X L. Fatigue behavior of corroded prestressed concrete beams. *Construction & Building Materials*, 2016, 106: 198–208
- Li F M, Yuan Y S, Li C Q. Corrosion propagation of prestressing steel strands in concrete subject to chloride attack. *Construction & Building Materials*, 2011, 25(10): 3878–3885
- Zhao Y X, Xu X Y, Wang Y Z, Dong J F. Characteristics of pitting corrosion in an existing reinforced concrete beam exposed to marine environment. *Construction & Building Materials*, 2020, 234: 117392
- Buchner S, Lindsell P. Testing of prestressed concrete structures during demolition. In: Proceedings of the International Seminar on Structural Assessment. Watford: Butterworth & Company Publishers Limited, 1987: 46–54
- Zghayar E E, Mackie K R, Haber Z B, Potter W. Secondary anchorage in post-tensioned bridge systems. *ACI Structural Journal*, 2013, 110(4): 629–638
- Dai L Z, Chen Y, Wang L, Ma Y F. Secondary anchorage and residual prestressing force in locally corroded PT beams after strand fracture. *Construction & Building Materials*, 2021, 275: 122137
- Rashetnia R, Ghasemzadeh F, Hallaji M, Pour-Ghaz M. Quantifying prestressing force loss due to corrosion from dynamic structural response. *Journal of Sound and Vibration*, 2018, 433: 129–137
- Bagge N, Nilimaa J, Elfgren L. *In-situ* methods to determine residual prestress forces in concrete bridges. *Engineering Structures*, 2017, 135: 41–52
- JGJ 55-2011. Specification for Mix Proportion Design of Ordinary Concrete. Beijing: Ministry of Housing and Urban-Rural Construction of the People's Republic of China, 2011 (in Chinese)
- GB/T 25181-2019. Ready-mixed Mortar. Beijing: State Administration for Market Regulation (SAMR) & Standardization Administration of the People's Republic of China (SAC), 2019 (in Chinese)
- Dang C N, Floyd R W, Murray C D, Hale W M, Martí-Vargas J R. Bond stress-slip model for 0.6 in. (15.2 mm) diameter strand. *ACI Structural Journal*, 2015, 112(5): 625–634
- Hwan Oh B, Sung Kim E. Realistic evaluation of transfer lengths in pretensioned, prestressed concrete members. *ACI Structural Journal*, 2000, 97(6): 821–830
- Dai L Z, Chen H, Wang L, Ma Y F, Zhang J R. Transfer length prediction in pre-tensioned concrete beams under corrosive cracking. *Structures*, 2021, 30: 938–948
- Coronelli D, Castel A, Vu N A, François R. Corroded post-tensioned beams with bonded tendons and wire failure. *Engineering Structures*, 2009, 31(8): 1687–1697
- ACI 318-14. Building Code Requirements for Structural Concrete and Commentary. Farmington Hill: American Concrete Institute, 2011
- JTG 3362-2018. Codes for Design of Highway Reinforced Concrete and Prestressed Concrete Bridge and Culverts. Beijing: Ministry of Transport of the People's Republic of China (MOT), 2018
- Russell B W, Burns N H. Measurement of transfer lengths on pretensioned concrete elements. *Journal of Structural Engineering*, 1997, 123(5): 541–549
- Hwan Oh B, Sung Kim E, Cheol Choi Y. Theoretical analysis of transfer lengths in pretensioned prestressed concrete members. *Journal of Engineering Mechanics*, 2006, 132(10): 1057–1066
- Abdelatif A O, Owen J S, Hussein M F M. Modelling the prestress transfer in pre-tensioned concrete elements. *Finite Elements in Analysis and Design*, 2015, 94: 47–63
- Lubliner J, Oliver J, Oller S, Oñate E. A plastic-damage model for concrete. *International Journal of Solids and Structures*, 1989, 25(3): 299–326
- Dai L Z, Long D X, Wang L. Meso-scale modeling of concrete cracking induced by 3D corrosion expansion of helical strands. *Computers & Structures*, 2021, 254: 106615
- Xiong Q R, Wang X F, Jivkov A P. A 3D multi-phase meso-scale model for modelling coupling of damage and transport properties in concrete. *Cement and Concrete Composites*, 2020, 109: 103545
- Lee S H, Abolmaali A, Shin K J, Lee H D. ABAQUS modeling for post-tensioned reinforced concrete beams. *Journal of Building Engineering*, 2020, 30: 101273
- Rabczuk T, Belytschko T. Cracking particles: A simplified meshfree method for arbitrary evolving cracks. *International Journal for Numerical Methods in Engineering*, 2004, 61(13): 2316–2343
- Rabczuk T, Zi G, Bordas S, Nguyen-Xuan H. A simple and robust three-dimensional cracking-particle method without enrichment. *Computer Methods in Applied Mechanics and Engineering*, 2010, 199(37–40): 2437–2455
- Rabczuk T, Belytschko T. A three-dimensional large deformation

- meshfree method for arbitrary evolving cracks. *Computer Methods in Applied Mechanics and Engineering*, 2007, 196(29–30): 2777–2799
- 31. Rabczuk T, Zi G, Bordas S, Nguyen-Xuan H. A geometrically non-linear three-dimensional cohesive crack method for reinforced concrete structures. *Engineering Fracture Mechanics*, 2008, 75(16): 4740–4758
 - 32. Ren H L, Zhuang X Y, Rabczuk T. A new peridynamic formulation with shear deformation for elastic solid. *Journal of Micromechanics and Molecular Physics*, 2016, 1(2): 1650009
 - 33. Ren H L, Zhuang X Y, Rabczuk T. A higher order nonlocal operator method for solving partial differential equations. *Computer Methods in Applied Mechanics and Engineering*, 2020, 367: 113132
 - 34. Ren H L, Zhuang X Y, Rabczuk T. A nonlocal operator method for solving partial differential equations. *Computer Methods in Applied Mechanics and Engineering*, 2020, 358: 112621
 - 35. Ren H L, Zhuang X Y, Oterkus E, Zhu H H, Rabczuk T. Nonlocal strong forms of thin plate, gradient elasticity, magneto-electro-elasticity and phase-field fracture by nonlocal operator method. *Engineering with Computers*, 2021: 1–45
 - 36. Ren H L, Zhuang X Y, Anitescu C, Rabczuk T. An explicit phase field method for brittle dynamic fracture. *Computers & Structures*, 2019, 217: 45–56
 - 37. Zhuang X Y, Ren H L, Rabczuk T. Nonlocal operator method for dynamic brittle fracture based on an explicit phase field model. *European Journal of Mechanics. A, Solids*, 2021, 90: 104380
 - 38. Li C Q, Yang S T, Saafi M. Numerical simulation of behavior of reinforced concrete structures considering corrosion effects on bonding. *Journal of Structural Engineering*, 2014, 140(12): 04014092
 - 39. Wang L, Li T, Dai L Z, Chen W, Huang K. Corrosion morphology and mechanical behavior of corroded prestressing strands. *Journal of Advanced Concrete Technology*, 2020, 18(10): 545–557
 - 40. Berto L, Simioni P, Saetta A. Numerical modelling of bond behaviour in RC structures affected by reinforcement corrosion. *Engineering Structures*, 2008, 30(5): 1375–1385
 - 41. Wang L, Zhang X H, Zhang J R, Yi J, Liu Y M. Simplified model for corrosion-induced bond degradation between steel strand and concrete. *Journal of Materials in Civil Engineering*, 2017, 29(4): 04016257